Thermal Neutron Scattering Law Evaluations for Zirconium Carbide and Critical Mass Calculations

J. L. Wormald[1*], J. C. Holmes[1], and M. L. Zerkle[1]

[1] Naval Nuclear Laboratory

PO Box 79, West Mifflin, PA 15122-0079, USA

jonathan.wormald@unnpp.gov, jesse.holmes@unnpp.gov, michael.zerkle@unnpp.gov

doi.org/10.13182/PHYSOR22-37273

ABSTRACT

Zirconium carbide (ZrC) is a candidate material for use in advanced high temperature reactors, including space nuclear thermal propulsion applications. Thermal neutron scattering laws (TSLs) are generated for carbon bound in ZrC, C(ZrC), and zirconium bound in ZrC, Zr(ZrC), using *ab initio* lattice dynamics methods. These evaluations are to be submitted for inclusion in ENDF/B-VIII.1 and use the incoherent approximation for inelastic scattering as well as the new mixed elastic scattering treatment. The application of disordered alloy theory is introduced to appropriately capture the isotopic composition of Zr and C in the elastic scattering cross section. Localized higher energy vibrations in the C(ZrC) phonon density of states that are separated from lower energy modes result in quantized oscillations in the inelastic contributions to the TSL with a significant likelihood of large energy down-scattering and up-scattering interactions, where the latter increases in probability with temperature. The quanta of energy transfer during neutron thermalization is substantially greater than classically expected within the thermal neutron energy range. MC21 critical mass calculations of ZrC mixtures with high-enriched uranium demonstrate an impact of the TSLs when compared to free-gas treatment for ^{235}U concentrations less than 0.2 g/cm^3. Additional MC21 critical mass calculations with homogenous mixtures of ZrC and reactor-grade graphite also demonstrate sensitivity to the ZrC TSL for thermal spectrum driven fission systems.

KEYWORDS: Thermal scattering law, zirconium carbide, moderator, phonons, ENDF/B

1. INTRODUCTION

Zirconium carbide (ZrC) is refractory material that is under consideration for use in advanced high temperatures reactors, typically as a fission product barrier in advanced TRISO fuel and as a corrosion barrier in space nuclear thermal propulsion (SNTP) applications [1,2]. During the Rover program ZrC was investigated at Los Alamos Scientific Laboratory as the base material for (U,Zr)C solid solution and ZrC-UC_2 composite fuel elements for NERVA-type SNTP concepts [3]. Composite (U,Zr)C-graphite fuel

* Corresponding author

elements with uranium content between 3.5 % – 11.5 % metal fraction were tested in Nuclear Furnace 1 (NF-1) to characterize material performance at high temperatures and extremely high power densities. While these historic experiments demonstrated that operating temperatures near 3000 K were achievable for the hours long durations required for SNTP applications, the impact of carbon chemical binding in ZrC on neutron thermalization was not considered despite the large volume fraction of carbides used in these systems.

In neutron transport calculations (e.g., Monte Carlo), ENDF thermal scattering laws (TSLs) capture the effect of chemical binding on thermalization of low-energy neutrons, typically neutrons less than 5 eV. The TSL, $S(\alpha,\beta)$, is a temperature-dependent distribution function describing the scattered states of the incident neutron that includes contributions from distinct (d) effects, due scattered wave interference from different scattering sites, and self (s) non-interference [4],

$$S(\alpha,\beta) = S_d(\alpha,\beta) + S_s(\alpha,\beta)\ . \tag{1}$$

As an ENDF convention, the momentum and energy exchange between the neutron and scattering medium are described by the unitless parameters α and β as,

$$\alpha = \frac{E+E'-2\mu\sqrt{E\cdot E'}}{Ak_BT} \tag{2}$$

$$\beta = \frac{E'-E}{k_BT}, \tag{3}$$

where μ is the scattering cosine, A is the nuclide to neutron mass ratio, the incident and scattered neutron energies are E and E', k_B is the Boltzmann constant, and T is temperature of the material. In crystalline materials the TSL is computed with the phonon expansion [4,5],

$$S(\alpha,\beta) = \sum_p S^p(\alpha,\beta), \tag{4}$$

which is a summation over increasing orders of convolutions of the vibrational (phonon) spectra, with the integer p indicating the number of phonons emitted and absorbed in the scattering process. Elastic scattering corresponds to $p = 0$, whereas $p > 0$ contributions represent inelastic scattering. In the ENDF thermal scattering sub-library, TSL material evaluations are conventionally generated in the incoherent approximation whereby distinct effects on inelastic scattering are neglected. Within this approximation, the double-differential scattering cross section is related to the TSL using Fermi's Golden rule as [4],

$$\frac{\partial^2\sigma}{\partial\Omega\partial E'} = \frac{1}{4\pi k_BT}\sqrt{\frac{E'}{E}}\left(\sigma_{coh}\left(S_d^0(\alpha,\beta) + S_s^0(\alpha,\beta) + \sum_{p>0} S_s^P(\alpha,\beta)\right) + \sigma_{inc}S_s(\alpha,\beta)\right). \tag{5}$$

where σ_{coh} and σ_{inc} are the bound coherent and incoherent potential scattering cross sections of the nuclide.

Previous studies have indicated that ZrC may influence neutron thermalization and criticality [6]; however, ZrC TSL evaluations have not previously been made available in ENDF to support analyses of reactors using this material. In this work, the TSLs for carbon and zirconium bound in ZrC, represented as Zr(ZrC) and C(ZrC), respectively, are generated from phonon spectra derived from *ab initio* lattice dynamics (AILD) for inclusion in the ENDF/B-VIII.1 database. These TSLs were generated using the Full Law Analysis Scattering System Hub (FLASSH), which includes a generalized coherent elastic scattering routine [7]. To treat the effect of the isotopic composition of each element on elastic scattering, disordered alloy theory is introduced to the standard TSL evaluation methodology. MC21 critical mass calculations were used to

evaluate the impact of the TSL when compared to free-gas (FG) treatment and reactor-grade graphite (RxGr). Since ZrC has historically been paired with graphite in reactor systems, additional MC21 critical mass analyses for composites of ZrC and RxGr were performed.

2. COMPUTATIONAL METHODS FOR TSL

ZrC crystallizes in cubic rock-salt structure (space group Fm-3m), shown in Figure 1, where each element forms a face-centered cubic sublattice. *Ab initio* simulations of ZrC utilized the VASP electronic structure theory code [8] within the MedeA atomistic environment [9]. These simulations used plane-augmented wave potentials and a GGA-PBE exchange correlation functional [10,11]. A plane-wave energy of 500 eV and Monkhorst-Pack *k*-mesh of less than 1.9 nm^{-1} were used and found to provide energy convergence within 5 meV/atom. Initially, the crystal geometry was optimized yielding a lattice parameter of 0.471017 nm in good agreement with the experimental value of 0.46983 nm [12].

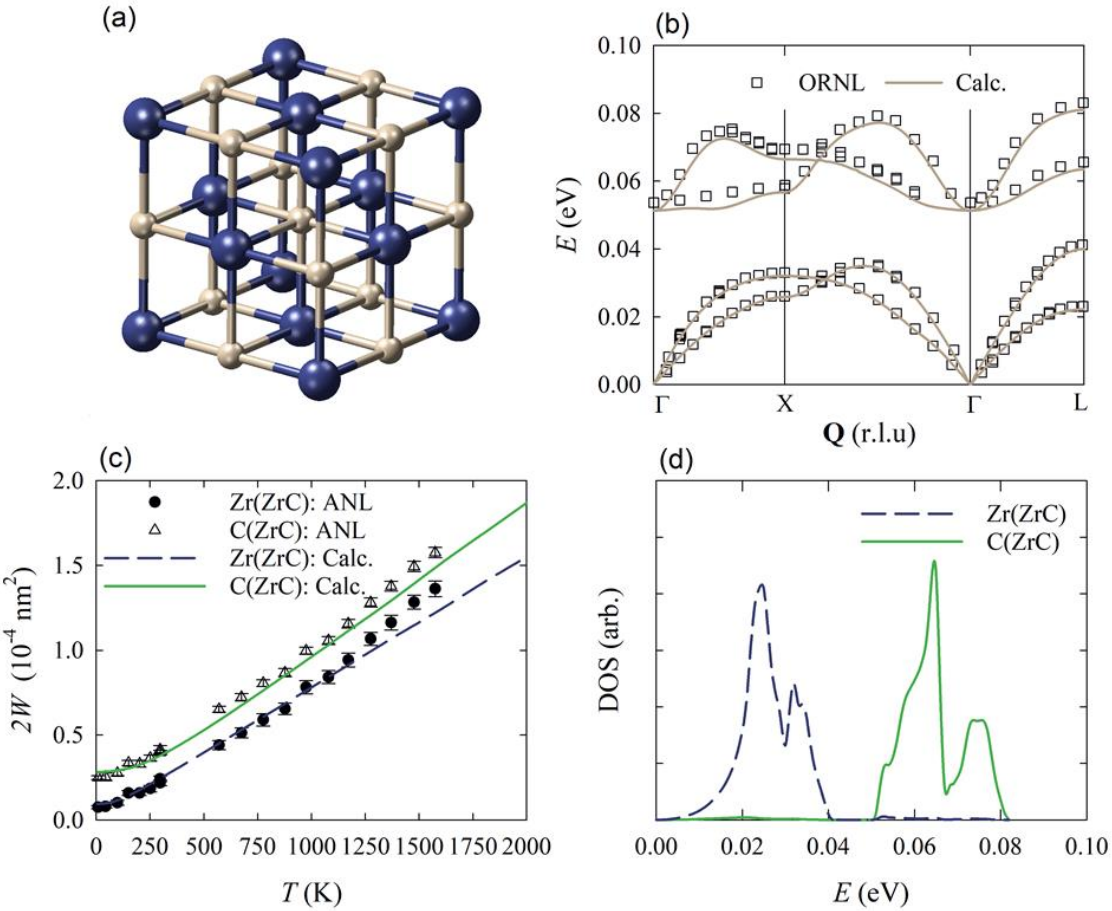

Figure 1. (a) ZrC crystal unit cell with Zr blue (large) and C brown (small). (b) AILD Phonon dispersion relations compared to inelastic neutron scattering measurements at Oak Ridge National Laboratory (ORNL) [13]. (c) Debye-Waller coefficient for C(ZrC) and Zr(ZrC) compared to neutron diffraction analysis at Argonne National Laboratory (ANL) [14]. (d) Partial phonon DOS for C(ZrC) and Zr(ZrC).

The phonon density of states (DOS) represents the fundamental input to the generation of the TSL in the incoherent approximation and was generated for ZrC using AILD methods, described in Ref. [15], whereby

Hellmann-Feynman forces are extracted from VASP supercell calculations as the input to the PHONON lattice dynamics code [16]. Phonons for ZrC were generated for a $4 \times 4 \times 4$ supercell using 10^6 phonon momentum vectors randomly sampled within the Brillouin zone to generate the phonon DOS. As illustrated in Figure 1, phonon dispersion relations, which map the phonon momentum and energy states, are in good agreement with experiment [13]. Debye-Waller coefficients, also shown Figure 1, are in reasonable agreement with experiment [14]. These temperature dependent coefficients provide an integral validation of the phonon DOS and are direct inputs to the elastic and inelastic contributions to the TSL as a representation of the vibrational mean square displacement.

The partial phonon DOS for Zr and C bound in ZrC are illustrated in Figure 1. The C(ZrC) phonon spectrum is observed to be relatively localized and separated in energy from the Zr(ZrC) spectrum in part due to the large mass disparity between C and Zr. The localized high-energy modes of C(ZrC) are suitable to cause a quantum harmonic oscillator effect in the TSL, which has been observed in the ENDF TSLs of uranium mononitride and several metal hydrides (e.g., PuH_2, ZrH_x, and YH_2) [17-20]. In contrast to the featureless TSLs of typical materials at higher energy transfer, quantum oscillator materials exhibit regularly structured TSLs as a function β for large energy transfer with special consequences to neutron thermalization, which will be discussed for ZrC in the subsequent section.

TSLs for natural C(ZrC) and Zr(ZrC) were generated in the incoherent approximation as File 7 evaluations in ENDF-6 format [21] using the FLASSH code [7]. The phonon spectra used in the TSL evaluation for each element were calculated using their elemental masses, which is reasonable based on the similar masses among Zr nuclides and the low abundance of ^{13}C. Each TSL was evaluated with a phonon order of 300 in Eq. (4) for temperatures ranging from 77 K to 2000 K, consistent with the maximum temperature of crystalline and reactor-grade graphite ENDF/B-VIII.0 TSL evaluations [20]. Since ^{13}C and ^{91}Zr have both incoherent and coherent contributions to potential scattering, both the C(ZrC) and Zr(ZrC) evaluations use mixed elastic scattering treatment [22]. Inelastic scattering on MT=4 and incoherent elastic scattering on MT=2 are tabulated with the elemental average total free atom cross section and bound incoherent elastic cross section, respectively. Table I and Table II lists total scattering cross sections and nuclide mass for C and Zr derived from ENDF/B-VIII.0 nuclide evaluations [20] as well as isotopic abundances from NIST [23]. Total scattering cross sections corresponds to File 3 MT=2 of the nuclide evaluations at a neutron energy of 0.0253 eV. Incoherent scattering cross section from Sears [24] and coherent scattering cross section are also listed. The coherent cross sections for C and Zr are calculated using disordered alloy theory.

Disordered alloy theory [25], original developed for diffraction in metal alloys, may be applied to capture interference effects from random distribution of different nuclides for each element among the crystal lattice sites. Coherent elastic scattering on MT=2 is computed under the assumption of a non-textured polycrystalline material, such that the cross section for a cubic material is given as,

$$\sigma_{coh,el}(E) = \frac{1}{E}\sum_{E_I<E}\frac{1}{G_I}\left|F(\boldsymbol{G}_I)\right|^2, \tag{6}$$

where E_I and G_I are the Bragg energies and reciprocal lattice vectors, respectively, related by E_I. In disordered alloy theory, the structure factor for a cubic material is given as,

$$F(\boldsymbol{G}_I) = \sum_{\mu,j} f_j \bar{b}_{\mu,j} \exp(i\boldsymbol{G}_I \cdot \boldsymbol{R}_\mu) \exp\left(-W_{\mu,j}G_I^2\right), \tag{7}$$

where $\boldsymbol{R}_\mu$ are the atom positions for each site, μ, in the crystal unit cell, $W_{\mu,j}$ are the Debye-Waller coefficients, and f_j is the atom fraction of each nuclide, j, at each lattice site. The bound coherent scattering length for a nuclide, $\bar{b}_{\mu,j}$, is related to the bound coherent scattering cross section as $\sigma_{coh} = 4\pi\bar{b}^*\bar{b}$. In the present work a single Debye-Waller coefficient is used for each element such that coherent scattering is

dependent on the elemental average scattering length. A difference of around 1% in MT=2 for ZrC is found with this treatment relative to using an elemental average of the coherent cross section for each element.

Table I. Neutron mass ratio and free scattering cross sections for elemental carbon.

Nuclide	Abundance	A	σ_{tot} (b)	σ_{coh} (b)	σ_{inc} (b)
^{12}C	0.9893	11.89365	4.748167	4.748167	0
^{13}C	0.0107	12.89165	5.732169	5.43935741	0.29281159
Natural C		11.9043286	4.75869582	4.75532245	0.00309601

Table II. Neutron mass ratio and free scattering cross sections for elemental zirconium.

Nuclide	Abundance	A	σ_{tot} (b)	σ_{coh} (b)	σ_{inc} (b)
^{90}Zr	0.5145	89.1324	5.265975	5.265975	0
^{91}Zr	0.1122	90.1247	9.694484	9.547758128	0.14672587
^{92}Zr	0.1715	91.1155	7.025888	7.025888	0
^{94}Zr	0.1738	93.0996	8.611622	8.611622	0
^{96}Zr	0.028	95.0844	4.826874	4.826874	0
Natural Zr		90.43999307	6.63385741	6.5201180	0.01646390

3. RESULTS AND DISCUSSION

3.1. Thermal Scattering Law and Secondary Neutron Distributions

The inelastic contribution to the TSLs for C(ZrC) and Zr(ZrC) is illustrated in Figure 2 for 293.6 K and 2000 K. The Zr(ZrC) $S(\alpha,\beta)$ is dominated by low energy transfer for neutron scattering that approaches a FG behavior at high momentum transfer (i.e., α), which is typical of heavy nuclides in crystalline materials (e.g., U(UN) and Zr(ZrH_x)). Highly structured quantized oscillations, however, are observed in the $S(\alpha,\beta)$ of C(ZrC). These quantum oscillations occur at integer values of the average energy of the partial phonon spectra, approximately $\beta k_B T = 0.065$ eV, such that each integer quanta from $\beta = 0$ corresponds directly to the phonon order of the interaction. For low momentum transfer, illustrated with $\alpha = 0.0415$, 1-phonon interaction processes are dominant across the entire temperature range of the evaluation. However, as momentum transfer increases, discrete multi-phonon interactions become likely, most prominently for down-scattering. As temperature increases, high momentum transfer $S(\alpha,\beta)$ approaches the FG, but retains low amplitude oscillations even at 2000 K. In contrast to metal hydrides such as zirconium hydride where down-scattering interactions ($\beta < 0$) due to quantum oscillations are highly favored [17], up-scattering interactions are of a similar magnitude to low energy down-scattering events.

Secondary energy distributions for C(ZrC) and carbon in RxGr, C(RxGr), are compared for several incident neutron energies in Figure 3. Collision of epithermal neutrons with C(ZrC) at room temperature, as exemplified at $E = 1$ eV, result in larger energy loss due to quantum oscillations when compared to RxGr, which has a more conventional behavior approaching a FG in this energy range. At high temperatures near 2000 K, the effects of chemical binding on the secondary neutron energy for C(ZrC) and C(RxGr) are less pronounced in the epithermal range, with both compounds approximating the FG despite some remnants of quantized energy exchange in ZrC.

As the neutron energy approaches the energy range of the phonon spectra between 0.05 eV and 0.08 eV, near complete energy loss becomes probable. These unconventionally large energy transfers are characteristic of quantum oscillator materials but are highly improbable for conventional moderators or a FG. Quantized 1-phonon energy loss is forbidden for thermal neutrons below the 0.05 eV cutoff of the C(ZrC) phonon spectra such that thermalization due to collisions with carbon becomes inefficient. Whereas scattering with C(RxGr) in the thermal energy range (~0.0253 eV) is characterized by quasi-elastic energy events, large energy up-scattering events dominate scattering with C(ZrC) in this energy range. Consequently, C(ZrC) will promote a hardening of the thermal spectrum toward higher neutron energies that is divergent from the ideal Maxwell Boltzmann distribution approached with moderators such as RxGr. At low temperatures these large up-scattering events are 1-phonon energy transfers of nearly 0.065 eV; however, at high temperatures approaching 2000 K 2-phonon and 3-phonon energy transfers of around 0.13 eV and 0.2 eV, respectively, are also likely. Therefore, hardening of the thermal spectra is anticipated to accelerate with increasing temperature. Moreover, these large discrete energy transfers are the underlying mechanism for the large prompt negative moderator feedback coefficient of ZrH_x-moderated TRIGA reactors [26]. ZrC can be anticipated to provide similar effects.

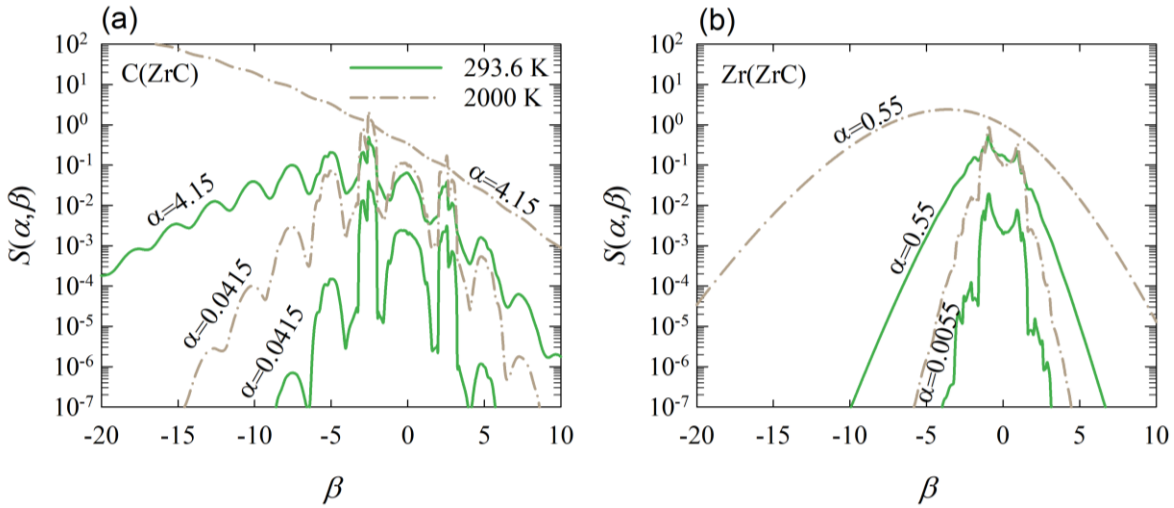

Figure 2. Inelastic contribution to the TSL for (a) C(ZrC) and (b) Zr(ZrC) evaluated at 293.6 K and 2000 K. The α and β values for each temperature are referenced to $k_BT = 0.0253$ eV. Oscillations in C(ZrC) $S(\alpha,\beta)$ occur at integer values of approximately $\beta k_BT = 0.065$ eV.

The total integrated cross section at 293.6 K for ZrC and the inelastic contributions from C and Zr at 293.6 K and 2000 K are illustrated in Figure 3. Due to the larger scattering cross section of Zr, inelastic scattering with Zr is generally more likely relative to C above the thermal neutron temperature (i.e., $E = k_BT$). Within this energy range, the inelastic cross section of C(ZrC) decreases abruptly near 0.065 eV as 1-phonon energy loss becomes energetically prohibited. In the $1/v$ low-energy range, scattering with C becomes increasingly dominant with increasing temperature. Accordingly, the increased cross section can be expected to facilitate the spectral hardening of the thermal neutron spectra through multi-phonon absorption observed at high temperatures in the secondary energy distributions for incident energies below 0.0253 eV.

3.2. Critical Mass Calculations

The sensitivity of criticality to the ZrC TSL was evaluated through minimum critical mass calculations using MC21 [27] for homogeneous mixtures of high-enriched uranium (HEU) metal and ZrC, RxGr, and a

homogenous mixture of RxGr and ZrC (labeled ZrC+RxGr) in bare spherical configurations. For the first and last case the effect of FG treatment for ZrC on k_{eff} was also computed. Thermal scattering data for MC21, which uses the direct method for sampling scattering outcomes [28], was generated with the NDEX nuclear data processing code [29,30]. A standard HEU composition was used with a total uranium density of 18.82342 g/cm^3. The 30% porous RxGr ENDF/B-VIII.0 TSL was selected for this study with a density of 1.589 g/cm^3 based on the theoretical graphite density of 2.27 g/cm^3 [31]. ZrC was modeled with the theoretical density of 6.61 g/cm^3 [1]. MC21 simulations were run with 10^6 particles per batch for 200 active and 40 discard batches, which is sufficient to converge k_{eff} to within approximately 10^{-5} for the current calculations. Each configuration was examined at room temperature (i.e., 293.6 K).

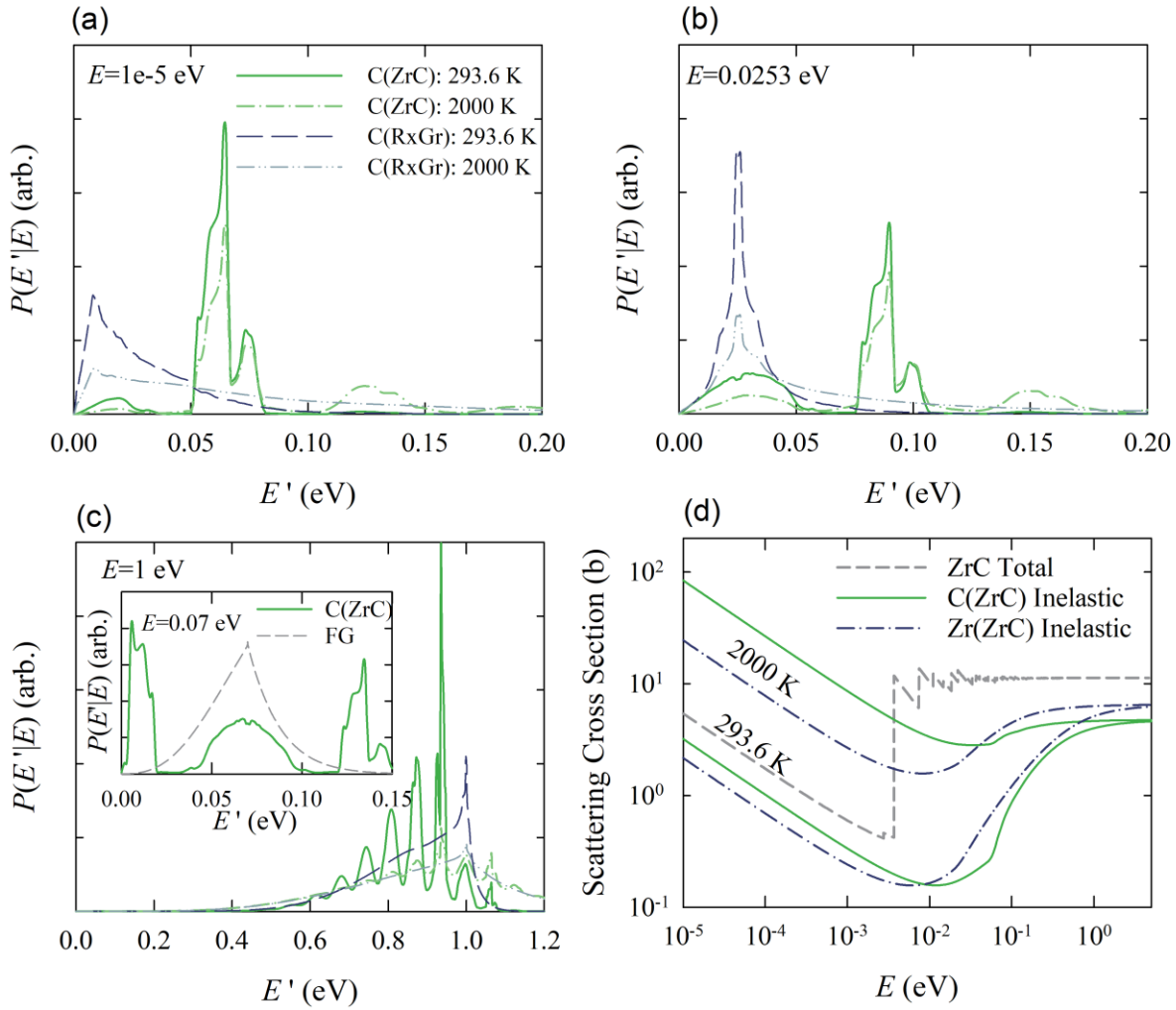

Figure 3. Secondary neutron energy distributions, $P(E'|E)$, for C(ZrC) generated with NDEX for incident neutron energies of (a) 10^{-5} eV, (b) 0.0253 eV, and (c) 1.0 eV. The scattered and incident neutron energies are E' and E. Each distribution is compared to C(RxGr), at 293.6 K and 2000 K. The $E = 0.07$ eV inset illustrates the unconventional quantized energy transfer in C(ZrC) relative to a FG treatment of the TSL. (d) The total scattering cross section of ZrC at 293.6 K is shown, as well as the inelastic scattering cross section for C(ZrC) and Zr(ZrC) at 293.6 K and 2000 K.

The critical mass as a function of ^{235}U loading density for bare spheres of HEU mixed with ZrC, RxGr, and a homogenous mixture of ZrC and RxGr are compared in Figure 4. The volume fraction of ZrC in the homogenous mixture of ZrC+RxGr was set to 0.35 based on the NF-1 tests [3]. For each configuration, the low-energy neutron spectra transition from an epithermal at a ^{235}U loading density of around 0.2 g/cm^3 to a thermal spectra at 0.02 g/cm^3. A corresponding divergence in the critical masses develops within this range. For the ZrC-based systems, the reactivity change between the ZrC TSL and FG treatment is calculated as,

$$\Delta\rho = \frac{1}{k_{\text{eff}}^{\text{FG}}} - \frac{1}{k_{\text{eff}}^{\text{TSL}}}. \tag{8}$$

This is illustrated in Figure 4 as a function of Zr/^{235}U rather than ^{235}U loading density for the purposes of relating the results to (U,Zr)C solid solution compositions studied in NF-1. Reactivity change is observed to yield a divergence from $\Delta\rho = 0$ above a Zr/^{235}U ratio of 10 – the same loading range as the divergence in the critical mass – indicating a sensitivity of to the TSL for thermal systems of both the pure ZrC and homogeneous ZrC+RxGr mixture. This Zr/^{235}U range overlaps the 10 – 30 range of (U,Zr)C NF-1 solid solutions fuel forms. Above 100 Zr/^{235}U (i.e., below 0.05 g/cm^3 ^{235}U) the room-temperature sensitivity of critical mass to the ZrC TSL compared to FG treatment is significant, on the order of several hundred pcm.

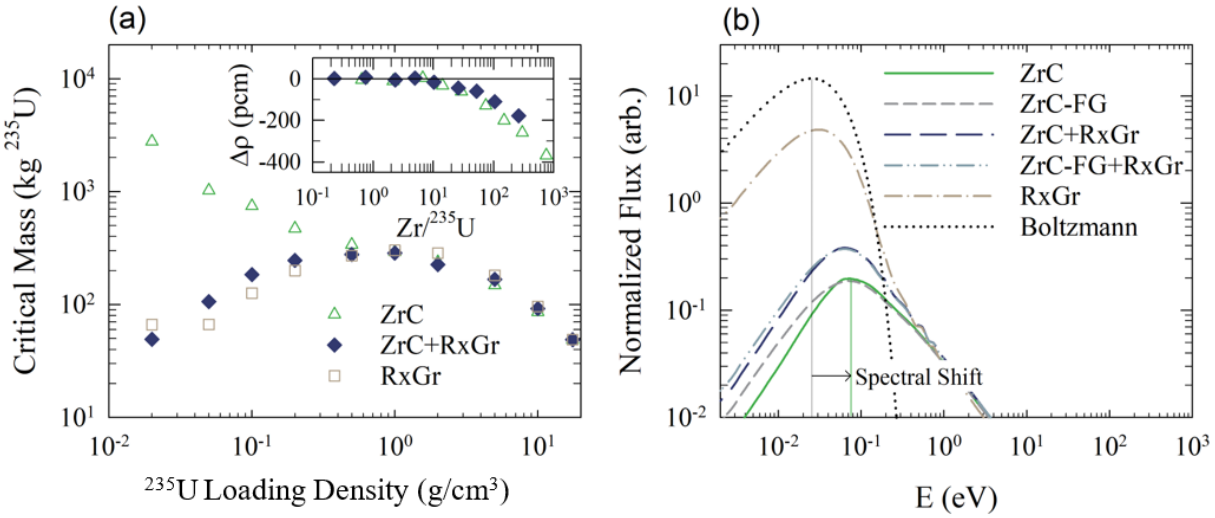

Figure 4. (a) Critical Mass as a function of ^{235}U loading density for bare sphere configurations of ZrC, RxGr, and the ZrC+RxGr homogenous mixture. The inset illustrates the change in reactivity for the ZrC TSL dataset compared to a FG treatment for this material. (b) Flux distributions in each configuration are compared for a select ^{235}U loading of 0.02 g/cm^3. The spectral shift between the Boltzmann distribution and ZrC illustrates the strong hardening effect caused by this material.

Increasing critical mass with lower ^{235}U loading density demonstrates that ZrC has limited efficacy as a solitary moderator. Conversely, RxGr has greater moderator efficiency with decreasing ^{235}U loading density but saturates at around 0.05 g/cm^3 such that the critical ^{235}U mass does not change appreciably for larger sphere sizes. The ZrC+RxGr homogenous mixture has a critical mass that is more characteristic of RxGr rather than ZrC; however, the critical mass of the mixture decreases less rapidly than RxGr and does not saturate in the examined loading range. This quantitative difference in behavior suggests a combined effect with ZrC+RxGr moderators that may influence reactor performance of TRISO or SNTP applications with significant volume fractions of ZrC.

To elucidate the critical mass and reactivity behavior in thermal neutron driven configurations, the thermal spectra of the critical mass configurations at a ^{235}U loading density of 0.02 g/cm^3 are compared in Figure 4. The RxGr spectra is highly thermal with a peak similar to the ideal Boltzmann distribution, whereas the ZrC spectra has substantial hardening with a peak around 0.073 eV. Moreover, ZrC+RxGr has a thermal spectra in between the RxGr and ZrC cases but more functionally characteristic of ZrC than RxGr despite the consistent trends in critical mass between the RxGr and ZrC+RxGr. In both ZrC-based systems, the use of a FG treatment in lieu of the ZrC TSL yields a more thermalized spectrum due to the prohibition of 1-phonon energy loss in ZrC below 0.05 eV as well as highly probable large energy up-scattering in the thermal energy range. Consequently, it can be presumed that in thermal systems the ZrC TSL is a significant driver of the thermal spectra and will tend to yield hardened spectra consistent with the expected physics of the secondary energy distributions. In mixed moderator applications where ZrC is the secondary moderator, as exemplified with the ZrC+RxGr system, the primary moderator may soften the spectra. This spectral softening in the exemplar ZrC+RxGr case is a competition between the discrete large energy up-scattering of ZrC and the near quasi-elastic scattering of RxGr within the thermal energy range.

4. CONCLUSIONS

TSL evaluations have been generated for C(ZrC) and Zr(ZrC) for inclusion in ENDF/B-VIII.1. The underlying phonon spectra, generated with AILD, have been validated against available experimental data as a first step toward validating the TSLs. As a result of a localized high-energy peak in the partial phonon spectrum, the inelastic contribution to the C(ZrC) TSL has regularly structured oscillations that result in quantized energy transfer during neutron thermalization but which are unconventional for non-hydrogenous materials. Critical mass calculations demonstrate that quantized up-scattering due to the C(ZrC) TSL causes substantial hardening of the thermal neutron spectrum for ZrC and homogenous mixtures with traditional moderator materials, such as ZrC with RxGr. Furthermore, criticality of thermal systems with Zr/^{235}U ratios greater than 10 are found to be sensitive to the ZrC TSL in comparison to FG treatments. The neutronic behavior of thermal-driven fission with large volume fractions of ZrC (e.g., NF-1) are anticipated to be influenced by the TSL of this material.

ACKNOWLEDGMENTS

The submitted manuscript has been authored by contractors of the US Government under contract No. DOE-89233018CNR000004. Accordingly, the US Government retains a non-exclusive, royalty-free license to publish or reproduce the published form of this contribution, or allow others to do so, for US Government purposes. This research made use of the resource of the High Performance Computing Center at Idaho National Laboratory, which is supported by the Office of Nuclear Energy of the U.S. Department of Energy and the Nuclear Science User Facilities under Contract No. DE-AC07-05ID14517.

REFERENCES

1. Y. Katoh, et al., “Properties of Zirconium Carbide for Nuclear Fuel Applications,” *J. Nucl. Mater.,* **441**, pp. 718-742 (2013).
2. National Academies of Sciences, Engineering, and Medicine, *Space Nuclear Propulsion for Human Mars Exploration*, The National Academic Press, Washington, DC, USA (2021).
3. L. L. Lyon, “Performance of (U,Zr)C-Graphite (Composite) and (U,Zr)C (Carbide) Fuel Elements in the Nuclear Furnace 1 Test Reactor”, LA-5398-MS, Los Alamos Scientific Laboratory (1973).
4. A. I. Hawari, “Modern techniques for inelastic thermal neutron scattering analysis,” *Nucl. Data Sheets*, **118**, pp. 172-175 (2014).
5. R. E. MacFarlane, “New Thermal Neutron Scattering Files for ENDF/B-VI Release 2,” LA-12639-MS, Los Alamos National Lab (1994).

6. F. C. Difilippo, and J. P. Renier, “Double Differential Neutron Scattering Cross Sections of Materials for Ultra High Temperature Reactors,” *Ann. Nucl. Energy*, **34**, pp. 130-139 (2007).
7. Y. Zhu and A. I. Hawari, “Full Law Analysis Scattering System Hub (FLASSH),” *Proceedings of PHYSOR 2018*, Canún, Mexico, April 22-26 (2018).
8. G. Kresse and J. Furthmüller, “Efficient iterative schemes for ab initio total energy calculations using a plane-wave basis set,” *Phys. Rev. B*, **54**, pp. 11169-11186 (1996).
9. MedeA version 3.0, Materials Design, Inc., San Diego, USA (2019).
10. G. Kresse and D. Joubert “From ultrasoft pseudopotentials to the projector augmented-wave method,” *Phys. Rev. B*, **59**, pp. 1758-1775 (1999).
11. J. P. Perdew, K. Burke and M. Ernzerhof, “Generalized gradient approximation made simple,” *Phys. Rev. Lett.*, **77**, pp. 3865-3868 (1996).
12. R. V. Sara, “The System Zirconium-Carbon,” *J. Am. Ceram. Soc.*, **48** (5), pp. 243-247 (1965).
13. H. G. Smith, N. Wakabayashi, and M. Mostoller, "Phonon Anomalies in Transition Metals, Alloys and Compounds," *Superconductivity in d- and f-band Metals*, Rochester, NY, Apr. 30 – May 1, pp. 223-249 (1976).
14. A. C. Lawson, et al., “Thermal Expansion of Atomic Vibrations of Zirconium Carbide to 1600 K,” *Philos. Mag.*, **87** (17), pp. 2507-2519 (2007).
15. A. I. Hawari, et al. “Ab initio generation of thermal neutron scattering cross sections,” *Proceedings of PHYSOR 2004*, Chicago, IL, April 25-29 (2004).
16. K. Parlinski, Z. Q. Li and Y. Kawazoe, “First-Principles Determination of the Soft Mode in Cubic ZrO_2,” *Phys. Rev. Lett.*, **78**, pp. 4063-4066 (1997).
17. J. Wormald, M. Zerkle, and J. Holmes, “Generation of the TSL for Zirconium Hydrides from Ab Initio Methods,” *J. Nucl. Eng.*, **2** (2), pp. 105-113 (2021).
18. M. L. Zerkle and J. C. Holmes, “The thermal neutron scattering law for hydrogen bound in plutonium dihydride and predicted critical mass for several configurations,” *Proceedings of the 2017 Nuclear Criticality Safety Division Topical Meeting*, Carlsbad, NM, Sep. 10-15 (2017).
19. M. Zerkle and J. Holmes, “A thermal neutron scattering law for yttrium hydride,” *EPJ Web of Conferences*, **146**, pp. 13005-13008 (2017).
20. D. A. Brown, et al., “ENDF/B-VIII.0: The 8th major release of the nuclear reaction data library with CIELO-project cross sections, new standards and thermal scattering data,” *Nucl. Data Sheets*, **148**, pp. 1-142 (2018).
21. M. Herman and A. Trkov, “Data Formats and Procedures for the Evaluated Nuclear Data File ENDF/B-VI and ENDF/B-VII,” BNL-90365-2009, Brookhaven National Laboratory (2009).
22. M. L. Zerkle, “TSL Mixed Elastic Scattering Format,” CSWEG, Nov. 30 – Dec. 4, 2020, https://indico.bnl.gov/event/7233/contributions/43822.
23. J. S. Coursey, et al., “Atomic Weights and Isotopic Compositions (version 4.1),” National Institute of Standards and Technology, http://physics.nist.gov/Comp (2015).
24. V. F. Sears, “Neutron scattering lengths and cross sections,” *Neutron News*, **29**, pp. 26-37 (1992).
25. W. Schweika, *Disordered Alloys*, Chapter 2, pp. 8-11, Springer-Verlag, Berlin, Germany (1998).
26. G. B. West, et al., “Behavior of TRIGA Reactors,” GA-7882; General Atomics (1967).
27. D. P. Griesheimer, et al. “MC21 v6.0 – A continuous-energy Monte Carlo Particle Transport Code with Integrated Reactor Feedback Capabilities,” *Ann. Nucl. Energy* **82**, pp. 29-40 (2015).
28. C. T. Ballinger, “The direct S(α,β) method for thermal neutron scattering,” *Proc. Int. Conf. on Math. and Comp. React. Phys. and Envron. Anal.*, Portland, Oregon, (1995).
29. J. L. Wormald, J. T. Thompson and T. H. Trumbull, “Implementation of an Adaptive Energy Grid Routine in NDEX for the Processing of Thermal Neutron Scattering Cross Sections,” *Ann. Nucl. Energy*, **149**, pp. 107773 (2020).
30. T. H. Trumbull, “Computational methods used to process thermal neutron scattering data for use in continuous energy Monte Carlo codes,” *Proceedings of PHYSOR 2016*, Sun Valley, ID, May 1-5 (2016).
31. D. D. L. Chung, “Review of Graphite,” *J. Mater. Sci.*, **37**, pp. 1475-1489 (2002).